Research Square

Preprints are preliminary reports that have not undergone peer review.
They should not be considered conclusive, used to inform clinical practice,
or referenced by the media as validated information.

Nup88-SENP3 axis coordinates ribosome biogenesis and CDK6-dependent proliferation in breast cancer

Ram Mishra

rkmishra@iiserb.ac.in

Indian Institute of Science Education and Research Bhopal https://orcid.org/0000-0002-9528-0476

Divya Bindra

Indian Institute of Science Education and Research Bhopal

Smit Patel

Indian Institute of Science Education and Research Bhopal

Drishiya Vats

Indian Institute of Science Education and Research Bhopal

Shruti Agrawal

Bansal Hospital https://orcid.org/0000-0002-3859-599X

Article

Keywords:

Posted Date: October 22nd, 2026

DOI: https://doi.org/10.21203/rs.3.rs-11232806/v1

License: This work is licensed under a Creative Commons Attribution 4.0 International License.
Read Full License

Additional Declarations: (Not answered)

Nup88-SENP3 axis coordinates ribosome biogenesis and CDK6-dependent proliferation in breast cancer

Divya Bindra[1], Smit Patel[1], Drishiya Vats[2], Shruti Agrawal[3], Ram Kumar Mishra[1]

[1]Department of Biological Sciences, Indian Institute of Science Education and Research Bhopal, Bhopal, Madhya Pradesh 462066 India

[2]Animal Facility, Indian Institute of Science Education and Research Bhopal, Bhopal, Madhya Pradesh 462066 India

[3]Department of Pathology, Bansal Hospital, Bhopal, Madhya Pradesh 462016 India

Abstract

Nup88 is frequently found overexpressed in human malignancies and is associated with aggressive tumor behavior. Yet the molecular details of elevated Nup88-dependent oncogenic growth remain poorly understood. Here, we report SENP3 as a functional determinant of Nup88-driven phenotypes in breast cancer. Patient datasets analyses revealed a strong positive association between Nup88 and SENP3 expression, and their coordinated abundance in breast tumor specimens. Enhancement in Nup88 levels in cells resulted in increased SENP3 expression. Conversely, Nup88 depletion reduced SENP3 abundance in a proteasome-dependent manner. Interestingly, modulation of SENP3 altered the intracellular distribution of Nup88, promoting its intranuclear and nucleolar accumulation. Concomitant increase in Nup88 and SENP3 levels enhanced pre-rRNA processing and increased levels of ribosomal proteins, indicative of modulated ribosome biogenesis. Enhanced Nup88 levels promoted cell cycle progression owing to increased CDK6 expression and activation of E2F-responsive programs. These effects were substantially attenuated following SENP3 depletion. In accordance, elevated Nup88 levels enhanced colony formation and tumor spheroid growth in vitro and promoted tumor expansion in in vivo mice model. Together, our findings uncover a previously unrecognised functional relationship between Nup88 and SENP3 in cancer. The Nup88-SENP3 axis provides an explanation to Nup88 level dependent biosynthetic, metabolic and proliferative alterations in cancer.

Introduction

Nup88 is frequently overexpressed in cancers and its abundance is associated with tumor aggressiveness and adverse clinical outcomes(1–3). Canonically, Nup88 is a component of the cytoplasmic face of the nuclear pore complex (NPC), where along with Nup214, it contributes to the regulation of exportin-1/CRM1-dependent transport (4–6). Non-conventional functions of Nup88 include mitotic regulation, spindle organization and regulation of chromosomal stability (7–10), thereby creating a favorable environment for malignant growth (3,11) .

The cytoplasmic face of the NPC hosts important components of the SUMOylation based protein-modification machinery. SUMO-specific peptidases (SENPs) are involved in maturation and deconjugation of SUMO moieties in the SUMOylation cycle (12,13). The class of nucleolar SENPs, SENP3 and SENP5 regulate the modification status of SUMOylation proteins involved in nucleolar rRNA processing and ribosomal subunit maturation (14–16). Particularly, perturbation of SENP3 activity disrupts ribosome biogenesis, underscoring its importance in nucleolar functions (15). Moreover, SENP3 is responsive to oxidative stress (17) and is crucial for cancer adaptation (18–21). SENP3 is dynamically regulated by cellular conditions and when dysregulated, it impacts tumor cell survival, proliferation and metabolic adaptation (22–24), suggesting that SENP3 exerts a broader influence on cancer-relevant cellular programs.

Here, we report a strong positive correlation between Nup88 and SENP3 overexpression in breast cancer. Their association alters rRNA biogenesis and 60S-pre-ribosomal assembly, enabling modulated cellular biosynthetic capacity. Further,

we demonstrate a previously unrecognised facet of Nup88 biology, where Nup88 regulates CDK6 driven pRb/E2F-mediated cell cycle phase transition providing proliferation potential to breast cancer cells.

Results

Nup88 and SENP3 levels positively correlate in breast cancer

To ascertain the clinical relevance of Nup88 in breast cancer, we analysed Nup88 expression pattern using CPTAC datasets. As compared to normal tissues, breast tumor samples exhibited significantly higher Nup88 levels (Fig. 1A). More detailed analysis revealed that Nup88 expression was significantly increased across Luminal, HER2-positive, and triple-negative breast cancer (TNBC) subtypes, compared to normal tissue (Fig. 1B). Highest levels of Nup88 in TNBC samples highlighted a potential association between Nup88 levels and aggressiveness of tumor subtype. Further, stratification by pathological stage indicated a positive correlation between Nup88 levels and tumor stage (Fig. 1C). Moreover, Kaplan-Meier survival analysis based on Nup88 expression levels suggested significantly reduced overall survival in patients with high Nup88 expression (Fig. 1D). Collectively, these observations support a potential role for Nup88 in driving tumor progression.

To identify the potential partners of Nup88 functionality in breast cancer, we performed a correlation-based network analysis using TCGA datasets. This analysis revealed an interconnected gene network of Nup88, where a SUMO-specific protease, SENP3, represented a significantly enriched and highly connected node (Fig. 1E). Moreover, correlation analyses across independent breast cancer datasets confirmed a strong

positive association between Nup88 and SENP3 expression (R = 0.59; Fig. 1F), indicating their coordinated regulation in tumors.

Furthermore, similar correlation analyses between Nup88 and other known SENP family members did not show any significant correlation (Fig. S1). Conversely, the correlation of SENP3 expression with other Nups from different subcomplexes within the NPC correlated poorly, except for a weak positive correlation with Nup214 ($R = 0.224$, $p < 0.0001$; Fig S2). However, the strongest positive correlation amongst the tested Nups was exhibited between Nup88 and SENP3 expression ($R = 0.634$, $p < 0.0001$; Fig. S1).

Finally, we examined the expression of Nup88 and SENP3 proteins in patient breast tumor tissues and autologous adjacent samples via immunohistology analysis. We observed a significant increase in Nup88 and SENP3 staining in tumor tissues with SENP3 expression pattern that broadly paralleled Nup88 expression (Fig. 1G,H,S3). Together, these observations identify SENP3 as a key Nup88-associated factor in breast cancer, providing a strong rationale for investigating a functional connection between Nup88 and SENP3 in breast cancer.

Nup88 stabilises SENP3 and undergoes SENP3-mediated relocalisation

To determine whether Nup88 can functionally regulate SENP3, we used MCF7 (Luminal) and MDA-MB-231 (TNBC) cells throughout this study to validate our observations made with clinical datasets. Expression of GFP-Nup88 in MCF7 cells resulted in an increase in SENP3 transcript levels (Fig. 2A), and a pronounced increase in SENP3 protein levels compared to GFP-expressing control cells (Fig. 2B). To

exclude potential tag-dependent effects, Nup88 was expressed with a Myc-tag. Expression of Myc-Nup88 resulted in elevation of SENP3 levels comparable to GFP-Nup88 (Fig. S4A). Further, flow cytometry analysis validated Nup88 overexpression dependent enhancement in SENP3 in both MCF7 and MDA-MB-231 (Fig. 2C-F) cells. Next, we examined if SENP3 reciprocally regulates Nup88 levels. We overexpressed SENP3 in MCF7 cells, and assessed endogenous Nup88 levels. Quantitative immunoblot analysis suggested no significant change in Nup88 levels in SENP3 overexpressing cells (Fig. 2G, S4B).

We next examined the effect of Nup88 depletion on SENP3 protein levels. Nup88 depletion in MCF7 cells resulted in a marked reduction in SENP3 protein abundance compared to control cells (Fig. 2H). We further hypothesized that Nup88 may regulate SENP3 stability through a proteasome-dependent mechanism. Accordingly, SENP3 levels in cells which reduced upon Nup88-depletion, were restored to normal levels when treated with the proteasome inhibitor, MG132 (Fig. 2H). Quantitative analysis revealed that SENP3 levels decreased by approximately 2.5-fold upon Nup88 depletion in the absence of MG132. However, SENP3 levels were comparable between MG132-treated control and Nup88-depleted cells (Fig. 2I). Flow cytometry analysis further validated the reduction in SENP3 upon Nup88 depletion (Fig S4C,D). These findings indicate that Nup88 is required for maintaining basal SENP3 protein levels by preventing proteasome-mediated degradation.

SENP3 is a resident nucleolar protein (15), a sub-cellular location distinctly different from Nup88 localisation domain. SENP3 did not regulate Nup88 levels, so we asked if SENP3 can govern the dynamic intracellular distribution of Nup88. Immunofluorescence analysis of mCherry-SENP3 expressing MCF7 cells, intriguingly revealed a fraction of endogenous Nup88 relocalising to the nucleolus (Fig. 2J, upper

panel). This observation raised the possibility of SENP3 governing Nup88 recruitment to nucleolar compartments. We further utilised doxycycline-inducible GFP-Nup88 expressing stable cells and co-expressed mCherry-SENP3. Following doxycycline treatment (0.5 μg/mL), a pronounced enrichment of GFP-Nup88 within the nucleolus was observed, with prominent colocalisation with SENP3, consistent with a SENP3 concentration-dependent recruitment (Fig. 2J, middle panel). To determine whether the catalytic property of SENP3 is necessary for this Nup88 redistribution, we utilised a catalytically inactive SENP3 mutant (C532A), referred to as SENP3m. Overexpression of mCherry-SENP3m also drove GFP-Nup88 within the nucleolar compartment with striking colocalisation with SENP3 (Fig. 2J, lower panel). Thus, SENP3-dependent recruitment of Nup88 to the nucleolus is independent of its catalytic activity. These observations suggest that Nup88 and SENP3 can form a regulatory axis in breast cancer that may influence oncogenic phenotypes.

Nup88-SENP3 axis promotes tumor proliferation in breast cancer

Next, we asked if a coordinated regulation by Nup88 and SENP3 can lead to measurable oncogenic outcomes like proliferation and tumor growth. We probed the contribution of a potential Nup88-SENP3 axis in breast cancer cell proliferation by assessing Ki67, a marker of active cell cycling. Nup88 overexpressing MDA-MB-231 cells markedly increased nuclear Ki67 staining compared with GFP controls (Fig. 3A), and quantification revealed significant increase in Ki67 levels. Interestingly, SENP3 depletion in Nup88-overexpressing cells reduced Ki67 levels comparable to control cells (Fig. 3B). Concurring observations were made for Ki67 levels, when Nup88 and SENP3 levels were altered in MCF7 cells (Fig. 3C). Flow cytometry analysis similarly

showed a rightward shift in Ki67 peak following Nup88 overexpression, and a shift moving closer to Ki67 peak observed in GFP expressing cells when SENP3 was depleted in Nup88 overexpressing cells (Fig. 3D). Together, these data indicated a functional role for the Nup88-SENP3 regulatory axis in cellular proliferation.

We next asked whether Nup88-driven proliferative activity confers a sustained clonogenic advantage. Nup88 overexpression in breast cancer cells increased total colony area by approximately three and two folds respectively in MDA-MB-231 and MCF7 cells as compared to GFP expressing cells, suggesting a clonogenic growth advantage. Noticeably, SENP3-depletion in Nup88 overexpressing cells substantially suppressed the clonogenic potential, indicating that SENP3 is a functional mediator of Nup88-driven clonal expansion (Fig. 3E-G). Further, we examined the importance of the Nup88-SENP3 axis in driving 3D-spheroid formation. Consistent with previous observations, Nup88-expressing MDA-MB-231 cells generated a larger mean spheroid area (~0.21 mm^2) as compared with GFP controls (0.07 mm^2). The spheroid area decreased to 0.10 mm^2 when SENP3 was depleted in the Nup88-overexpressing cells (Fig. 3H,I). Similarly in MCF7 cells, the mean spheroid area for control cells (0.11 mm^2), increased to 0.21 mm^2 upon Nup88-overexpression and returned to control values 0.10 mm^2 when SENP3 was depleted (Fig. 3J,K). Thus, the Nup88-SENP3 axis seems operational and effective in three-dimensional tumor-relevant context as well.

Nup88-SENP3 axis enhances tumor formation and progression in vivo

We next asked whether this relationship translates into tumor growth in vivo. In this context, we employed a subcutaneous xenograft model using doxycycline inducible MDA-MB-231 cells stably expressing GFP, Nup88, or Nup88 together with SENP3

depletion in immunocompromised NOD/SCID mice, following the experimental scheme shown in Fig. 4A and details mentioned in the methods section.

The tumors excised from the Nup88-overexpressing group of mice were visibly larger than those from control animals. Notably, concomitant SENP3 depletion significantly reduced this tumor-growth phenotype, indicating substantial attenuation of the Nup88-dependent growth advantage (Fig. 4B,C). Endpoint measurements for Nup88-overexpressing tumors indicated a mean weight of 2.15 ± 0.48 g and volume of 1,887.61 ± 192.61 mm^3, ~ 3-fold higher when compared with 0.79 ± 0.13 g and 576.15 ± 137.21 mm^3 in control tumors. When SENP3 is depleted in Nup88-overexpressing tumors, ~33% reduction in tumor weight and volume to 1.42 ± 0.54 g and 1,371.35 ± 548 mm^3, respectively (Fig. 4D,E) was noticed. These findings establish that the Nup88-SENP3 axis is also functional in tumor growth in vivo.

Interestingly, when xenografts were processed following the protocol mentioned in Fig. 4F, SENP3 and Ki67 levels were significantly higher in Nup88-overexpressing tumor regions in comparison with control tumors (Fig. 4G,H). Together, these findings provide functional validation of the Nup88-SENP3 axis operating to promote tumor growth and proliferation in vivo.

Nup88 regulates ribosome biogenesis in a SENP3 dependent manner

SENP3 in essence is a resident nucleolar protein and a regulator of nucleolar homeostasis and ribosomal maturation. Elevated SENP3 levels recruiting Nup88 to nucleolus (Fig. 2J) implicated the importance of Nup88-SENP3 axis in nucleolar

function and ribosome biogenesis, processes frequently upregulated in cancer to support sustained proliferation. In this regard, we performed Gene set enrichment analysis (GSEA) to examine how Nup88 provides a proliferative potential to cancer cells. This analysis revealed a strong positive enrichment score (NES=2.03) and significant enrichment for gene sets associated with ribosomal RNA (rRNA) processing in Nup88-overexpressing cells (Fig. 5A). RT-qPCR analysis revealed a marked increase in 47S pre-rRNA following Nup88 overexpression, consistent with enhanced rRNA production (Fig. 5B). Mature 28S rRNA was similarly increased, indicating that the elevation in precursor rRNA was accompanied by increased accumulation of mature rRNA (Fig. 5C). Moreover, SENP3 depletion substantially reduced the Nup88-dependent increase in both 47S pre-rRNA and 28S rRNA transcript levels (Fig. 5B,C), implicating SENP3 as an important mediator of Nup88-induced ribosome biogenesis response.

Furthermore, the transcripts encoding components of the 60S large ribosomal subunit, including *RPL28, RPL5* and *RPL11*, were significantly elevated upon Nup88 overexpression (Fig. 5D-F). This induction in the level of RPLs was markedly reduced following SENP3 knockdown in the Nup88-overexpressing background. We then asked whether transcriptional changes were accompanied by altered abundance and intracellular distribution of ribosomal proteins. We focused on RPL5, a core 60S ribosomal protein with established functions in ribosome assembly and nucleolar organization (25,26). As compared to low and diffused nucleolar staining of RPL5 in MDA-MB-231 cells under basal conditions, Nup88 induction resulted in overall increase in RPL5 abundance and accumulation within both nucleolar and cytoplasmic compartments (Fig. 5G). Flow cytometric analysis further confirmed the increase in RPL5 abundance, with Nup88-overexpressing cells displaying a distinct rightward shift

in RPL5 fluorescence relative to control. SENP3 depletion partially reversed this shift, reducing RPL5 levels towards baseline (Fig. 5H). Together, these findings indicate that the Nup88-SENP3 axis engages ribosome biogenesis at multiple levels.

Next, we performed polysome profiling with cell lysates to observe a distinct redistribution of ribosomal species upon Nup88 overexpression. Using puromycin as a positive control for polysome collapse, that induces accumulation of the pre-polysomal fractions, Nup88 overexpression resulted in a pronounced increase in the pre-polysome peaks, while polysome-associated fractions showed a modest alteration relative to control cells (Fig. 5I). This suggests a remodeling of ribosome organization upon Nup88 overexpression. Analysis of different polysome fractions for the presence of the ribosomal protein RPL5 indicated increased RPL5 abundance in the polysome-associated fractions, upon Nup88-overexpression (Fig. 5J,S6A). This redistribution was attenuated following SENP3 depletion in Nup88 overexpressing background, although RPL5 remained detectable in the corresponding ribosomal fractions.

We next investigated the potential involvement of PELP1, a nucleolar scaffold protein implicated in ribosome assembly and pre-60S subunit maturation (27,28), whose function is regulated by SENP3-mediated modification (16,29). The gene network analysis of Nup88 in breast cancer found PELP1 as a strongly associated node (Fig S6B), with a direct correlation analysis depicting strong correlation between Nup88 and PELP1 ($R = 0.51$; Fig. 5K). Interestingly, PELP1 protein abundance increased to ~5.3-fold upon GFP-Nup88 expression as compared to GFP-expressing control (Fig. 5L), indicating that Nup88 positively regulates PELP1 levels. SENP3 depletion produced only a modest reduction in PELP1 abundance to ~4.6-fold, corresponding to ~13% decrease relative to Nup88-overexpressing cells. This may point towards both SENP3-

dependent and additional SENP3-independent mechanisms regulating Nup88-mediated modulation of PELP1. We next assessed PELP1 localisation dynamics in MCF7 cells. In GFP control cells, PELP1 was predominantly found diffused inside nucleoplasm and nucleolus (Fig. 5M, upper panel). However, Nup88 overexpression redistributed PELP1, with reduced nucleolar signal but increased nucleoplasmic accumulation (Fig. 5M, lower panel), indicating regulation of PELP1 dynamics by increased Nup88. These observations underscore the complexity of the Nup88-SENP3 axis mediated regulation on nucleolar function and ribosomal output in cancer cells.

Nup88-mediated acceleration through G1-S phase is CDK6 and SENP3-dependent

After substantiating that the Nup88-SENP3 axis promotes ribosome biogenesis, we probed the involvement of cyclin-dependent kinase 6 (CDK6), a key regulator of the G1-S transition (30) and a signaling node that can be influenced by nucleolar SENP-dependent mechanisms (31). As compared to GFP control, Nup88 overexpression caused a marked increase in CDK6 protein levels (Fig. 6A). Notably, depletion of SENP3 substantially decreased this induction, indicating that CDK6 upregulation downstream of Nup88 is dependent on SENP3.

To determine whether Nup88-associated changes extend beyond CDK6 to broader cell cycle transcriptional programs, we performed GSEA. Both the E2F target (NES=2.59) and G2/M checkpoint (NES=1.98) gene sets were significantly enriched in Nup88-high cells (Fig. 6B,C), consistent with activation of transcriptional programs associated with cell cycle progression. Given the established role of CDK6-dependent

Rb phosphorylation in releasing E2F transcription factors (32,33), an increase in E2F-responsive transcripts *CCNE1*, *TK1* and *NOP56* was observed in Nup88-overexpressing cells (Fig. 6D-F), whereas their expression is substantially reduced in SENP3 depleted but Nup88-overexpressing cells.

To assess any alteration in cell cycle dynamics due to CDK6 induction and E2F activation, GFP, GFP-Nup88 and GFP-Nup88 cells depleted of SENP3 were synchronised in G1 phase with the CDK4/6 inhibitor, Palbociclib, and released. and examined for cell cycle kinetics by flow cytometry (Fig. 6G). Immediately after release (0 hours post release, 0 hpr), bulk of the cells across all conditions remained in G1, confirming effective and comparable synchronisation (Fig. S7). But 12 hpr, Nup88-overexpressing cells displayed a more rapid redistribution into later cell cycle phases (from ~46% in GFP control to ~53% in GFP-Nup88 expressing cells in S-phase), indicating accelerated transition to S-phase. This phenotype was attenuated by SENP3 depletion, which resulted in a relative accumulation of cells in earlier phases (from ~29% in GFP-Nup88 expressing cells to ~37% in SENP3 depleted GFP-Nup88 expressing cells) and delayed cell cycle progression (Fig. 6H,I). Further, after Palbociclib synchronisation-release, status of Rb phosphorylation was assessed. Nup88 overexpression resulted in increased phosphorylation of Rb (pRb-S780), whereas SENP3 depletion significantly diminished pRb generation (Fig. 6J). These observations validate activation of the CDK6-Rb pathway downstream of Nup88-SENP3 axis that mediates enhanced G1-S transition.

Discussion

Functions of many nucleoporins, including Nup88, extend beyond their canonical roles in nucleocytoplasmic transport (3,34–36). Nup88 is recognised as a cancer-associated nucleoporin (1,2), although mechanisms underlying its contribution to tumor progression remain inadequately understood. Our analyses demonstrate Nup88 as a consistently elevated protein in breast cancer, irrespective of subtype or disease stage and identify its increased expression associated with adverse patient prognosis. SENP3, localised to nucleolus, is a SUMO-specific protease with well-established roles in rRNA processing, ribosome maturation, and nucleolar organisation (15,16,29). Moreover, enhanced SENP3 expression and function is reported in glioma, head and neck, gastric, and ovarian cancers (24). The strong positive correlation between Nup88 and SENP3 expression across breast cancer patient tissues, thus, aligns this clinically relevant Nup88-SENP3 association with increased biosynthetic needs of cancer cells. Consequently, we uncover a previously uncharacterised role for Nup88 in coupling its overexpression to the biosynthetic adaptation of proliferating cancer cells and its regulation by a functional relationship between Nup88 and SENP3. The ability of SENP3 to influence the intracellular distribution of Nup88 further provides a spatiotemporal clue about the involvement of Nup88-SENP3 axis in reorganisation of the nucleolus.

Ribosome production is extensively rewired during oncogenic transformation to sustain increased cellular demands (37,38). Moreover, the importance of SENP3 in PELP1-dependent 60S-pre-ribosomal particle assembly and transport is well recognised (16,39). We report here that the Nup88-SENP3 axis governs the coordinated changes

observed across synthesis of rRNA, ribosomal components and PELP1 localisation. Increased production of rRNA and ribosomal proteins, together with the accumulation of the nucleolar pool of RPL5 is consistent with enhanced availability of ribosomal components at the site of pre-ribosome assembly. The simultaneous increase of RPL5 in cytoplasm further suggests an expansion of the cellular ribosomal protein pool when the Nup88-SENP3 axis is engaged. This may also reflect consensus with the previously observed function of the Nup88-Nup214 subcomplex in the nuclear export of pre-60S ribosome subunits (40), linking Nup88 to multiple stages of ribosome maturation. Interestingly, co-expression of Nup214 in Nup88 overexpression background was previously observed to ameliorate multinuclear phenotypes in cells in culture (7), suggesting that the relative abundance of Nup88 and its associated nucleoporins may influence cellular outcomes. In contrast, the weak correlation between Nup214 and SENP3 in breast cancer indicates that the Nup88-SENP3 axis associated oncogenic outcomes have strong and specific Nup88 contributions. Interestingly, Nup62 copies Nup88 expression pattern in head and neck cancer and stabilizes Nup88 to influence the proliferative, apoptotic, and pro-inflammatory pathways (41). A poor correlation score between Nup62 and SENP3 in breast cancer further emphasizes the context-dependent contribution of Nup88 dysregulation in imparting tumorigenic potential to cells. The dynamic intracellular distribution of PELP1 under the influence of elevated Nup88 parallels the heterogeneous nuclear and cytoplasmic patterns of PELP1 localisation associated with cellular state and tumors, including breast cancer (42,43). Altered PELP1 abundance and redistribution accompanying Nup88 dysregulation may therefore reflect remodeling of the ribosome biogenesis machinery imposed by malignant growth. Taken together, we find that increased Nup88 levels are consistent with SENP3-integrated enhancement of the

ribosome biogenesis program to support the elevated biosynthetic demands of sustained proliferation in cancer.

Bypassing cell cycle checkpoints and accelerated cell cycle phase transitions have been one of the mechanisms operational in cancers (44). Emerging evidence suggests that proliferating cells must align their enhanced biosynthetic capacity with cell cycle progression events (37). This coupling between ribosome biogenesis and cell cycle transitions is crucial, as cells must achieve sufficient growth before committing to division, and its dysregulation causes aberrant proliferation commonly seen in aggressive cancers (38,45). We observe that dysregulated Nup88 also facilitates accelerated G1-S phase transition. Moreover, previous literature implicates alterations in Nup88 levels and stabilisation of enhanced Nup88 proteins in mitotic regulation (7,10). Perhaps, Nup88 influences the fidelity of cell division through cyclin-dependent kinases and transcriptional reprogramming at distinct cell cycle phases. In addition, alterations in global and specific SUMOylation and dysregulated SUMO-specific proteases, including SENP3, are common in tumors (24,46). Notably, SUMOylation of CDK6 by SUMO1, but not SUMO2/3, was shown to stabilise CDK6 and affect cell cycle and glioma progression (47). In our study, Nup88-mediated SENP3 regulation was associated with CDK6-dependent accelerated G1-S phase transition; however, because SENP3 preferentially deSUMOylates SUMO2/3, our findings place the SENP3-dependent regulation of CDK6 within a broader landscape of SUMO-linked cell cycle control. Accordingly, Nup88 functions as a molecular conduit capable of coordinating cellular growth programs and proliferative signaling in tumors.

Succinctly, our findings extend the functional repertoire of Nup88 and identify a Nup88-SENP3 regulatory axis that connects nucleoporin dysregulation with nucleolar organization and cell cycle regulation (Fig. 7). This axis provides a framework for understanding how elevated Nup88 supports the growth and proliferation of breast cancer cells. Our observations with Nup88 also open avenues for detailed future investigations of nucleoporins at nuclear envelope and nucleolus in coordinating a synchrony between cell cycle and cellular biosynthetic demands.

Materials and Methods

Plasmids

Plasmids pEGFP-C1-Nup88 (#64283), pcDNA3.1-Nup88 (#64281), and pEBG-PELP1 (#65209) were obtained from Addgene. The pLVX-TetOne-Puro vector, used for stable cell line preparation, was a kind gift from Dr. Jomon Joseph, NCCS, Pune, India. GFP-tagged Nup88 was subcloned from the pEGFP-C1-Nup88 construct into pLVX-TetOne-Puro using AgeI and BamHI restriction sites. shRNA plasmids were obtained from Sigma, Mission human genome shRNA library. SENP3 and its catalytic mutant SENP3(C532A) were subcloned from RGS-SENP3 (Addgene #18048) and RGS-SENP3m (Addgene #18714) constructs into the pmCherry-C1 vector between SacI and SalI sites. All constructs were verified by Sanger sequencing.

Breast tumor sample collection and immunohistology analysis (IHC/IF)

5 μm paraffin-embedded breast tumor sections mounted on poly-L-lysine coated slides were obtained from Bansal Hospital, Bhopal, India. The study was performed in accordance with approval from the Institute Ethics Committee of the Indian Institute of Science Education and Research Bhopal, India (IISERB/IEC/2016/Meeting-I/04). Sections were deparaffinised overnight at 65 °C, treated with xylene, and rehydrated through gradient concentrations of ethanol (100%, 95%, 70%, 50%), and finally distilled water. Antigen retrieval was done by boiling the tissue in Tris-EDTA buffer (pH 9.0) for 15 min. For DAB-based IHC, samples were power blocked with 10% hydrogen peroxide solution for 15 min at room temperature. Then, primary antibodies against Nup88 and SENP3 were incubated for 1 h at RT in separate sections of the same sample, followed by secondary antibody incubation for 15 min, PolyExcel poly-HRP and DAB development. Sections were counterstained with hematoxylin, washed, dried and mounted. For IF, after antigen retrieval, sections were blocked with 5% normal goat serum (NGS) for 1 h at RT. Samples were then incubated with primary antibodies for 1.5 h,

washed thrice, followed by appropriate Alexa Fluor secondary antibodies for 30 min at RT. Nuclear counter stain was performed and samples were mounted using DAPI containing Fluoroshield mounting medium (Sigma-Aldrich, F6057). Images were acquired using Olympus FV3000 confocal laser scanning microscope with a 20× objective and analysed using ImgaeJ/Fiji. Total 10 patient samples were used for the study and the details of these tissues obtained from breast cancer patients are provided in Supplementary Table 1.

Cell culture

HEK293T (CRL-3216), MCF-7 (HTB-22) and MDA-MB-231 (HTB-26) cells were obtained from ATCC and routinely maintained under standard tissue culture conditions at 37 °C in a humidified incubator with 5% CO2. Cells were cultured in Dulbecco's Modified Eagle Medium (DMEM; Gibco #11995) supplemented with 10% fetal bovine serum (FBS; Gibco #A5256801) and 100 units/ml penicillin-streptomycin (Gibco #15240).

Lentivirus production and generation of stable cell lines

HEK293T cells were transfected with the respective transfer plasmids, pLVX-TetOne-Puro-GFP-Nup88 or pLKO.1 shRNA plasmid and packaging plasmids- psPAX2 and pMD2.G at a 10:5:1 ratio using polyethyleneimine (PEI) following the standard protocol. After 12 h, the media was replaced with fresh DMEM media containing 10% FBS and antibiotics. Viral supernatants were collected after at 24 and 48 h, clarified by centrifugation, filtered through a 0.45 µm filter and stored at -80° C until further use. MCF-7 and MDA-MB-231 cells were transduced with respective lentiviral particles in the presence of 8 µg/mL polybrene (Sigma-Aldrich, TR-1003). After 48 h, transduced cells were selected with 0.5 µg/mL puromycin (Sigma-Aldrich, P9620) for 72 h. Doxycycline (Sigma, D5207) was used to induce expression of desired constructs in successfully transduced cells.

Western blotting

Cells were lysed using RIPA lysis buffer (50 mM Tris pH 7.5, 10 mM EDTA, 1 mM EGTA, 150 mM NaCl, 1% Triton X 100, 0.2% Sodium deoxycholate) supplemented with 1× Protease inhibitor cocktail and 100 mM PMSF. Cell lysates were sonicated and centrifuged at maximum speed to collect the supernatant. The supernatant was quantified using Bradford assay, and samples were prepared by adding 6X SDS sample buffer and boiled for 10 min at 100° C. The proteins separated by SDS-PAGE were transferred onto an activated PVDF membrane and blocked with 5% (w/v) BSA, followed by probing with suitable primary and secondary antibodies. Detection of bands was performed using the LI-COR Odyssey infrared imaging system (LI-COR Biosciences, Model: 9120). Detailed list of antibodies used is provided in Supplementary Table 2.

RNA isolation and Quantitative RT-PCR

Total RNA was isolated using Helix Biosciences RNA isolation kit (#FATRK001). 1 µg of total RNA was reverse transcribed to cDNA by iScript DNA synthesis kit (BioRad #17088) as per the manufacturer's instructions. RT-PCR was performed using SYBR Green PCR master mix (iTaq Universal SYBR Green Supermix, BioRad) on QuantStudio 5 (Applied Biosystems, Thermo Fisher Scientific). Actin gene was used for normalisation, and the relative transcript level was calculated by CT value ($2^{-\Delta\Delta CT}$). Ordinary one-way ANOVA was used to compare the differences in the gene expression, and p-value < 0.05 was considered significant. The primers used are listed in Supplementary Table 3.

Immunofluorescence

MCF-7 and MDA-MB-231 cells were cultured on sterile glass coverslips and transfected/treated as indicated. Cells were fixed using 4% paraformaldehyde for 15 min and permeabilised with phosphate-buffered saline (PBS) containing 0.1% Triton X-100 for 10 min at RT. Cells were subsequently blocked with 3% NGS for 30 min at RT. Primary antibodies

were diluted in PBS supplemented with 2% NGS and incubated overnight at 4 °C. After three washes with PBS, cells were incubated for 1 h at RT with Alexa Fluor-conjugated (488, 568, or 647) secondary antibodies, followed by three washes again with PBS. Coverslips were mounted onto glass slides using Fluoroshield mounting medium containing DAPI. Images were acquired using FV3000 confocal laser scanning microscope (Olympus) and processed using ImageJ/Fiji software.

Antibody based detection by flow cytometry

Cells were harvested following doxycycline induction where applicable and fixed with 4% paraformaldehyde for 15 min at RT. Fixed cells were permeabilised with 0.1% Triton X-100 for 5 min, then washed twice and then blocked with 3% NGS for 15 min at 4 °C. Cells were incubated with appropriate primary antibodies for 1 h at RT, then washed twice, followed by incubation with Alexa Fluor 568-conjugated secondary antibody for 30 min. After washing, fluorescence was measured using the BD FACSAria III system (BD Biosciences) and assessed by FlowJo software.

Cell cycle analysis by flow cytometry

Cells were induced with doxycycline where applicable, and for G1-phase synchronisation, treated with 1 μM Palbociclib (MedChem Express #HY50767) for 24 h, then changed with fresh media to enable recovery for appropriate time. Cells were subsequently harvested and fixed in ice-cold 70% ethanol at 4 °C. Cells were then washed twice and stained with staining solution containing propidium iodide (50 μg/mL; Sigma-Aldrich, P4170) and RNase A (50 μg/mL) in PBS for 30 min at RT. Further, cells were subjected to flow cytometric acquisition using the BD FACSAria™ III system (BD Biosciences) and FlowJo software for quantification.

Colony formation assay

Inducible MCF-7 and MDA-MB-231 cells were seeded at 2,000 cells per well in six-well plates and allowed to adhere for 12 h, then induced with doxycycline (0.5 µg/mL) for 15 days, with fresh doxycycline every alternate day. Cells were fixed with 4% paraformaldehyde for 15 min at RT, stained with 0.05% crystal violet in methanol for 15 min, washed, and air-dried prior to imaging. Colony formation was documented and quantified using ImageJ/Fiji software.

Spheroid assay

Inducible MCF-7 and MDA-MB-231 cells were seeded at 2,000 cells/well in 96-well plates precoated with 2% agarose and cultured in complete medium with doxycycline where applicable. Cells were allowed to form spheroids for 72 h and maintained for 6 days. Image acquisition and analysis were performed using high-content screening (HCS) imaging system (Thermo Fisher Scientific) and spheroid growth was quantified using ImageJ/Fiji.

Mice xenograft tumor analysis

For the study, female NOD/SCID mice (6-8 weeks old, healthy) were housed under standard laboratory conditions (20-25 °C, 12 h light/dark cycle, 60-70% relative humidity). The experimental protocol was reviewed and approved by the Institutional Animal Ethics Committee (IAEC) of IISER Bhopal (2025-IISERB-7.5-IAEC). Animal experiments were conducted in compliance with the guidelines provided by the Committee for Control and Supervision of Experiments on Animals (CCSEA, Govt. of India). At the end of the study, mice were euthanized by isoflurane inhalation followed by cervical dislocation.

Tumorigenic potential was evaluated in female NOD/SCID mice (6-8 weeks old) by subcutaneous implantation of 3×10^6 inducible MDA-MB-231 cells expressing either GFP control, GFP-Nup88 or GFP-Nup88 with SENP3 depletion background, resuspended in DMEM containing 10% fetal bovine serum and admixed 1:1 with growth factor-reduced Matrigel. Doxycycline (2 mg/mL) supplemented with 5% sucrose was administered continuously in

drinking water after tumor establishment over a period of initial 7 days. Tumor growth was monitored by calliper measurements, and tumor volumes (V) were calculated using the modified ellipsoid formula, $V = ½ \times \text{length} \times \text{width}^2$. At 4 weeks, tumors were excised, weighed, measured and processed for histopathological immunofluorescence analyses of Ki67 and SENP3.

Bioinformatics analyses

Gene expression and protein expression data from TCGA and CPTAC, respectively, were obtained using GEPIA3(48) and UALCAN (49), and gene expression correlations were analysed using GEPIA3. Survival analysis was performed using OncoLnc (http://www.oncolnc.org). For gene set enrichment analysis (GSEA), rRNA processing, E2F target, and G2/M hallmark gene sets were obtained from MSigDb database (50). Pre-ranked gene lists were generated based on differential expression between Nup88-high and Nup88-low groups and analysed using GSEA software (51). Enrichment was assessed using normalized enrichment score (NES), nominal *P* value, and false discovery rate (FDR q-value).

Data analysis and statistics

Data are presented as mean ± SEM from three biological replicates unless otherwise indicated. Statistical tests are specified in the respective figure legends, with $P \leq 0.05$ considered as statistically significant. Significance was denoted as $^{*}P \leq 0.05$, $^{**}P \leq 0.01$, $^{***}P \leq 0.001$, $^{****}P \leq 0.0001$, ns = not significant. GraphPad Prism 11 was used for all analyses. Image analysis and processing were done using ImageJ/Fiji software, and immunoblot band quantitation were done using GelQuant.NET.

Acknowledgements

We thank Dr. Jomon Joseph, NCCS, Pune for help with resources and valuable insights. We thank Dr. Atul Samaiya, Bansal Hospital, Bhopal for aiding in procuring breast cancer samples. We thank the members of the Nup and SUMO Biology Group (NSBG) for discussions. We acknowledge the Central Instrumentation Facility, Indian Institute of Science Education and Research Bhopal for confocal microscopy (DST FIST facility – Live cell imaging), flow cytometry and DNA sequencing facilities. Illustrations and schematics in this study were created with BioRender.com.

Author Contributions

D.B. designed and performed all experiments, analysed and interpreted the data, and wrote the manuscript. R.K.M. supervised the study, contributed to experimental design and data interpretation, and wrote the manuscript. D.B. and S.P. performed experiment and analyses of patient tissue samples. D.B. and D.V. performed in vivo mice experiments. S.A. provided cancer patient tissue samples and associated clinical information and helped in patient data interpretation.

Data Availability

All the data supporting the findings in this study are included in the article and the supplementary information.

Competing Interests

The authors declare no competing interests.

Ethics Approval

Breast tumor specimens were collected after obtaining informed consent from the patients. The study was performed in accordance with approval from the Institute Ethics Committee (IEC) of the Indian Institute of Science Education and Research Bhopal, India (IISERB/IEC/2016/Meeting-I/04). All procedures involving mice for xenograft studies were reviewed and approved by the Institutional Animal Ethics Committee (IAEC) of IISER Bhopal (2025-IISERB-7.5-IAEC). Animal experiments were conducted in compliance with the guidelines of the Committee for Control and Supervision of Experiments on Animals (CCSEA, Govt. of India).

Funding

D.B. was a recipient of research fellowship from PMRF. S.P. received fellowship from UGC. This work was funded by research grants CRG/2020/000496 from SERB, IIRPSG-2024-01-01766 from ICMR, and intramural support from IISER Bhopal.

References

1. Martínez N, Alonso A, Moragues D, Pontón J, Schneider J. The Nuclear Pore Complex Protein Nup88 Is Overexpressed in Tumor Cells. Cancer Res. 1999 Nov 1;59(21):5408-11. PMID: 10554006.
2. Agudo D, Gómez-Esquer F, Martínez-Arribas F, Núñez-Villar MJ, Pollán M, Schneider J. Nup88 mRNA overexpression is associated with high aggressiveness of breast cancer. Int J Cancer. 2004 May 1;109(5):717–20. doi:10.1002/ijc.20034 PubMed PMID: 14999780.
3. Li J, Zhao J, Li Y. Multiple biological processes may be associated with tumorigenesis under NUP88-overexpressed condition. Genes Chromosomes Cancer. 2017 Feb 1;56(2):117–27. doi:10.1002/gcc.22417 PubMed PMID: 27636375.
4. Bernad R, van der Velde H, Fornerod M, Pickersgill H. Nup358/RanBP2 Attaches to the Nuclear Pore Complex via Association with Nup88 and Nup214/CAN and Plays a Supporting Role in CRM1-Mediated Nuclear Protein Export. Mol Cell Biol. 2004 Mar 1;24(6):2373–84. doi:10.1128/mcb.24.6.2373-2384.2004 PubMed PMID: 14993277.
5. Fornerod M, Van Deursen J, Van Baal S, Reynolds A, Davis D, Murti KG, et al. The human homologue of yeast CRM1 is in a dynamic subcomplex with CAN/Nup214 and a novel nuclear pore component Nup88. EMBO J. 1997 Feb 17;16(4):807-16. doi: 10.1093/emboj/16.4.807.
6. Xylourgidis N, Roth P, Sabri N, Tsarouhas V, Samakovlis C. The nucleoporin Nup214 sequesters CRM1 at the nuclear rim and modulates NFκB activation in

Drosophila. J Cell Sci. 2006 Nov 1;119(21):4409–19. doi:10.1242/jcs.03201 PubMed PMID: 17032737.

7. Hashizume C, Nakano H, Yoshida K, Wong RW. Characterization of the role of the tumor marker Nup88 in mitosis. Mol Cancer. 2010 May 24;9. doi:10.1186/1476-4598-9-119 PubMed PMID: 20497554.

8. Naylor RM, Jeganathan KB, Cao X, Van Deursen JM. Nuclear pore protein NUP88 activates anaphasepromoting complex to promote aneuploidy. Journal of Clinical Investigation. 2016 Feb 1;126(2):543–59. doi:10.1172/JCI82277 PubMed PMID: 26731471.

9. Makise M, Nakamura H, Kuniyasu A. The role of vimentin in the tumor marker Nup88-dependent multinucleated phenotype. BMC Cancer. 2018 May 3;18(1). doi:10.1186/s12885-018-4454-y PubMed PMID: 29724197.

10. Zhao JS, Shi S, Qu HY, Keckesova Z, Cao ZJ, Yang LX, et al. Glutamine synthetase licenses APC/C-mediated mitotic progression to drive cell growth. Nat Metab. 2022 Feb 1;4(2):239–53. doi:10.1038/s42255-021-00524-2 PubMed PMID: 35145325.

11. Makise M, Uchimura R, Higashi K, Mashiki Y, Shiraishi R, Shutoku Y, et al. Overexpression of the nucleoporin Nup88 stimulates migration and invasion of HeLa cells. Histochem Cell Biol. 2021 Nov 1;156(5):409–21. doi:10.1007/s00418-021-02020-w PubMed PMID: 34331103.

12. Hang J, Dasso M. Association of the human SUMO-1 protease SENP2 with the nuclear pore. Journal of Biological Chemistry. 2002 May 31;277(22):19961–6. doi:10.1074/jbc.M201799200 PubMed PMID: 11896061.

13. Nayak A, Müller S. SUMO-specific proteases/isopeptidases: SENPs and beyond. Genome Biol. 2014 Jul 31;15(7):422. doi:10.1186/s13059-014-0422-2 PubMed PMID: 25315341.
14. Yun C, Wang Y, Mukhopadhyay D, Backlund P, Kolli N, Yergey A, et al. Nucleolar protein B23/nucleophosmin regulates the vertebrate SUMO pathway through SENP3 and SENP5 proteases. Journal of Cell Biology. 2008 Nov 17;183(4):589–95. doi:10.1083/jcb.200807185 PubMed PMID: 19015314.
15. Haindl M, Harasim T, Eick D, Muller S. The nucleolar SUMO-specific protease SENP3 reverses SUMO modification of nucleophosmin and is required for rRNA processing. EMBO Rep. 2008;9(3):273–9. doi:10.1038/embor.2008.3 PubMed PMID: 18259216.
16. Finkbeiner E, Haindl M, Muller S. The SUMO system controls nucleolar partitioning of a novel mammalian ribosome biogenesis complex. EMBO Journal. 2011 Mar 16;30(6):1067–78. doi:10.1038/emboj.2011.33 PubMed PMID: 21326211.
17. Huang C, Han Y, Wang Y, Sun X, Yan S, Yeh ETH, et al. SENP3 is responsible for HIF-1 transactivation under mild oxidative stress via p300 de-SUMOylation. EMBO Journal. 2009 Sep 16;28(18):2748–62. doi:10.1038/emboj.2009.210 PubMed PMID: 19680224.
18. Yu Y, Bao W, Chen J, Li Y, Gao Y. SENP3 drives colorectal cancer progression by enhancing GDF15 expression. Int J Colorectal Dis. 2026 Mar 13;41(1):80. doi:10.1007/s00384-026-05120-y
19. Zhou Z, Wang M, Li J, Xiao M, Chin YE, Cheng J, et al. SUMOylation and SENP3 regulate STAT3 activation in head and neck cancer. Oncogene. 2016 Nov 10;35(45):5826–38. doi:10.1038/onc.2016.124 PubMed PMID: 27181202.

20. Zhu Y, Zhang J, Yu L, Xu S, Chen L, Wu K, et al. SENP3 promotes tumor progression and is a novel prognostic biomarker in triple-negative breast cancer. Front Oncol. 2023 Jan 9;12. doi:10.3389/fonc.2022.972969

21. Chen X, Li D, Su Q, Ling X, Yang Y, Liu Y, et al. SENP3 mediates the deSUMOylation and degradation of YAP1 to regulate the progression of triple-negative breast cancer. Journal of Biological Chemistry. 2024 Oct 1;300(10). doi:10.1016/j.jbc.2024.107764 PubMed PMID: 39270822.

22. Wang P, Qiu J, Fang Y, Li S, Liu K, Cao Y, et al. SENP3 inhibition suppresses hepatocellular carcinoma progression and improves the efficacy of anti-PD-1 immunotherapy. Cell Death Differ. 2025 May 1;32(5):959–72. doi:10.1038/s41418-024-01437-9 PubMed PMID: 39755756.

23. Yang P, Liu Y, Qi YC, Lian ZH. High SENP3 Expression Promotes Cell Migration, Invasion, and Proliferation by Modulating DNA Methylation of E-Cadherin in Osteosarcoma. Technol Cancer Res Treat. 2020;19. doi:10.1177/1533033820956988 PubMed PMID: 33030103.

24. Long X, Zhao B, Lu W, Chen X, Yang X, Huang J, et al. The Critical Roles of the SUMO-Specific Protease SENP3 in Human Diseases and Clinical Implications. Frontiers in Physiology. Frontiers Media S.A.; 2020. doi:10.3389/fphys.2020.558220

25. Matsumori H, Watanabe K, Tachiwana H, Fujita T, Ito Y, Tokunaga M, et al. Ribosomal protein L5 facilitates rDNA-bundled condensate and nucleolar assembly. Life Sci Alliance. 2022 Jul 1;5(7). doi:10.26508/lsa.202101045 PubMed PMID: 35321919.

26. Nicolas E, Parisot P, Pinto-Monteiro C, De Walque R, De Vleeschouwer C, Lafontaine DLJ. Involvement of human ribosomal proteins in nucleolar structure

and p53-dependent nucleolar stress. Nature Communications . 2016 Jun 6;7. doi:10.1038/ncomms11390 PubMed PMID: 27265389.

27. Gordon J, Kaminski AM, Bommu SR, Skrajna A, Petrovich RM, Pedersen LC, et al. PELP1 coordinates the modular assembly and enzymatic activity of the rixosome complex. Sci Adv. 2025 Jul 25;11(30):eadw4603. doi: 10.1126/sciadv.adw4603. Epub 2025 Jul 25. PMID: 40712028

28. Sareddy GR, Vadlamudi RK. PELP1: Structure, biological function and clinical significance. Gene. Elsevier B.V.; 2016. p. 128–34. doi:10.1016/j.gene.2016.03.017 PubMed PMID: 26997260.

29. Castle CD, Cassimere EK, Denicourt C. LAS1L interacts with the mammalian Rix1 complex to regulate ribosome biogenesis. Mol Biol Cell. 2012 Feb 15;23(4):716–28. doi:10.1091/mbc.E11-06-0530 PubMed PMID: 22190735.

30. Tigan AS, Bellutti F, Kollmann K, Tebb G, Sexl V. CDK6-a review of the past and a glimpse into the future: From cell-cycle control to transcriptional regulation. Oncogene. Nature Publishing Group; 2016. p. 3083–91. doi:10.1038/onc.2015.407 PubMed PMID: 26500059.

31. Dönig J, Mende H, Davila Gallesio J, Wagner K, Hotz P, Schunck K, et al. Characterization of nucleolar SUMO isopeptidases unveils a general p53-independent checkpoint of impaired ribosome biogenesis. Nat Commun. 2023 Dec 1;14(1). doi:10.1038/s41467-023-43751-9 PubMed PMID: 38065954.

32. Sherr CJ, Roberts JM. Living with or without cyclins and cyclin-dependent kinases. Genes and Development. 2004. p. 2699–711. doi:10.1101/gad.1256504 PubMed PMID: 15545627.

33. Narasimha AM, Kaulich M, Shapiro GS, Choi YJ, Sicinski P, Dowdy SF. Cyclin D activates the Rb tumor suppressor by mono-phosphorylation. Elife. 2014 Jun 4;3. doi:10.7554/elife.02872

34. Merigliano C, Ryu T, Cibulka J, Rawal CC, See CD, Mitra A, et al. Off-pore Nup98 condensates mobilize heterochromatic breaks and exclude Rad51. Mol Cell. 2025 Jun 19;85(12):2355-2373.e11. doi:10.1016/j.molcel.2025.05.012 PubMed PMID: 40480227.

35. Bindra D, Mishra RK. In Pursuit of Distinctiveness: Transmembrane Nucleoporins and Their Disease Associations. Frontiers in Oncology. Frontiers Media S.A.; 2021. doi:10.3389/fonc.2021.784319 PMID: 34970494.

36. Ibarra A, Hetzer MW. Nuclear pore proteins and the control of genome functions. Genes and Development. Cold Spring Harbor Laboratory Press; 2015. p. 337–49. doi:10.1101/gad.256495.114 PubMed PMID: 25691464.

37. Hwang SP, Denicourt C. The impact of ribosome biogenesis in cancer: from proliferation to metastasis. NAR Cancer. Oxford University Press; 2024. doi:10.1093/narcan/zcae017 PubMed PMID: 38633862.

38. Elhamamsy AR, Metge BJ, Alsheikh HA, Shevde LA, Samant RS. Ribosome Biogenesis: A Central Player in Cancer Metastasis and Therapeutic Resistance. Cancer Research. American Association for Cancer Research Inc.; 2022. p. 2344–53. doi:10.1158/0008-5472.CAN-21-4087 PubMed PMID: 35303060.

39. Raman N, Weir E, Müller S. The AAA ATPase MDN1 Acts as a SUMO-Targeted Regulator in Mammalian Pre-ribosome Remodeling. Mol Cell. 2016 Nov 3;64(3):607–15. doi:10.1016/j.molcel.2016.09.039 PubMed PMID: 27814492.

40. Bernad R, Engelsma D, Sanderson H, Pickersgill H, Fornerod M. Nup214-Nup88 nucleoporin subcomplex is required for CRM1-mediated 60 S preribosomal

nuclear export. Journal of Biological Chemistry. 2006 Jul 14;281(28):19378–86. doi:10.1074/jbc.M512585200 PubMed PMID: 16675447.

41. Singh U, Bindra D, Samaiya A, Mishra RK. Overexpressed Nup88 stabilized through interaction with Nup62 promotes NF-κB dependent pathways in cancer. Front Oncol. 2023 Feb 9;13. doi:10.3389/fonc.2023.1095046. PMID: 36845732

42. Vadlamudi RK, Manavathi B, Balasenthil S, Nair SS, Yang Z, Sahin AA, et al. Functional implications of altered subcellular localization of PELP1 in breast cancer cells. Cancer Res. 2005 Sep 1;65(17):7724–32. doi:10.1158/0008-5472.CAN-05-0614 PubMed PMID: 16140940.

43. Girard BJ, Knutson TP, Kuker B, McDowell L, Schwertfeger KL, Ostrander JH. Cytoplasmic localization of proline, glutamic acid, leucinerich protein 1 (PELP1) induces breast epithelial cell migration through up-regulation of inhibitor of κb kinase ϵ and inflammatory cross-talk with macrophages. Journal of Biological Chemistry. 2017 Jan 6;292(1):339–50. doi:10.1074/jbc.M116.739847 PubMed PMID: 27881676.

44. Matthews HK, Bertoli C, de Bruin RAM. Cell cycle control in cancer. Nature Reviews Molecular Cell Biology. Nature Research; 2022. p. 74–88. doi:10.1038/s41580-021-00404-3 PubMed PMID: 34508254.

45. Tsai RYL, Pederson T. Connecting the nucleolus to the cell cycle and human disease. FASEB Journal. FASEB; 2014. p. 3290–6. doi:10.1096/fj.14-254680 PubMed PMID: 24790035.

46. Eifler K, Vertegaal ACO. SUMOylation-Mediated Regulation of Cell Cycle Progression and Cancer. Trends in Biochemical Sciences. Elsevier Ltd; 2015. p. 779–93. doi:10.1016/j.tibs.2015.09.006 PubMed PMID: 26601932.

47. Bellail AC, Olson JJ, Hao C. SUMO1 modification stabilizes CDK6 protein and drives the cell cycle and glioblastoma progression. Nat Commun. 2014 Jun 23;5. doi:10.1038/ncomms5234 PubMed PMID: 24953629.

48. Kang YJ, Pan L, Liu Y, Rong Z, Liu J, Liu F. GEPIA3: Enhanced drug sensitivity and interaction network analysis for cancer research. Nucleic Acids Res. 2025 Jul 7;53(W1):W283–90. doi:10.1093/nar/gkaf423 PubMed PMID: 40396370.

49. Chandrashekar DS, Karthikeyan SK, Korla PK, Patel H, Shovon AR, Athar M, et al. UALCAN: An update to the integrated cancer data analysis platform. Neoplasia (United States). 2022 Mar 1;25:18–27. doi:10.1016/j.neo.2022.01.001 PubMed PMID: 35078134.

50. Liberzon A, Subramanian A, Pinchback R, Thorvaldsdóttir H, Tamayo P, Mesirov JP. Molecular signatures database (MSigDB) 3.0. Bioinformatics. 2011 Jun;27(12):1739–40. doi:10.1093/bioinformatics/btr260 PubMed PMID: 21546393.

51. Subramanian A, Tamayo P, Mootha VK, Mukherjee S, Ebert BL, Gillette MA, et al. Gene set enrichment analysis: A knowledge-based approach for interpreting genome-wide expression profiles. Proc Natl Acad Sci U S A. 2005 Oct 25;102(43):15545-50. doi: 10.1073/pnas.0506580102. Epub 2005 Sep 30. PMID: 16199517

Figure Legends

Figure 1. Nup88 is overexpressed in breast cancer and positively correlates with SENP3 expression. A, Nup88 protein expression in breast cancer tumor samples compared to normal tissue. B, Nup88 expression across breast cancer subtypes (Luminal, HER2+, and TNBC) compared to normal tissue. C, Nup88 expression across different stages of breast cancer progression. Statistical significance in (A-C) was determined using unpaired t-test. D, Kaplan-Meier overall survival analysis of patients stratified based on Nup88 expression levels (low vs high). Statistical significance was determined using the log-rank test ($p = 0.03$). p-values are indicated in each case. E, Network analysis of Nup88-correlated genes in breast cancer (BRCA dataset), highlighting SENP3 as a significantly associated node. F, Scatter plot analysing correlation between Nup88 and SENP3 expression in breast cancer samples ($R = 0.59$, $p < 0.0001$). G, Immunohistochemical (IHC, left, Scale bar, 100 μm) and immunofluorescence (IF, right, Scale bar, 50 μm) analysis of Nup88 and SENP3 levels in breast cancer patient cohort. H, Pearson correlation analysis between Nup88 and SENP3 fluorescence intensities determined from IF ($R = 0.91$, $p < 0.001$, $n=10$).

Figure 2. Nup88 regulates SENP3 stability and undergoes dynamic relocalisation through association with SENP3. A, Semi-quantitative PCR analysis and quantification of SENP3 levels in cells expressing GFP or GFP-Nup88. B, Immunoblot showing SENP3 levels upon GFP-Nup88 overexpression in MCF7. C, Flow cytometry histograms showing SENP3 expression in MCF7 with either GFP or GFP-Nup88 overexpression. D, Quantification of mean fluorescence intensity (MFI) of SENP3 under indicated conditions as in (C). E, Flow cytometry histograms showing SENP3

796 expression in MDA-MB-231 with either GFP or GFP-Nup88 overexpression. F,
797 Quantification of MFI of SENP3 under indicated conditions as in (E). Statistical
798 significance in (A,D,F) was determined using unpaired t-test. G, Quantification of
799 Nup88 levels upon SENP3 overexpression in MCF7. Statistical significance was
800 determined using one-way ANOVA followed by Dunnett's multiple comparisons test. H,
801 Immunoblot analysis of SENP3 levels upon shRNA-mediated Nup88 knockdown
802 with/without MG132 (10 μM, 8 h) in MCF7 cells. I, Quantification of (H) showing fold
803 change in SENP3 levels relative to control conditions. Statistical significance was
804 determined using two-way ANOVA. Bars indicate mean ± S.E.M. (*$p < 0.05$, **$p < 0.01$,
805 ***$p < 0.001$, ****$p < 0.0001$). J, Representative immunofluorescence image of MCF7
806 cells expressing either mCherry-SENP3 and stained for endogenous Nup88, or co-
807 expressing mCherry-SENP3 and GFP-Nup88, or co-expressing catalytic mutant
808 SENP3 (C532A) and GFP-Nup88. Line scans for images in merge panel are shown on
809 the right. Scale bar, 10 μm.

810

811 **Figure 3. The Nup88-SENP3 axis promotes tumor proliferation in breast cancer**
812 **cells.** A, Immunofluorescence analysis of MDA-MB-231 cells expressing GFP or GFP-
813 Nup88 (green) and stained for Ki67 (red) with DAPI (blue). Scale bar, 10 μm. B-C,
814 Quantification of Ki67 fluorescence intensity in MDA-MB-231 (B) and MCF7 (C) cells
815 under the indicated conditions, respectively. D, Flow cytometry histogram depicting
816 Ki67 expression in MDA-MB-231 cell populations under indicated conditions. E,
817 Representative images of colony formation assay in MDA-MB-231 (upper) and MCF7
818 (lower) cells under indicated conditions. F-G, Quantification of colony-forming ability in
819 MDA-MB-231 (F) and MCF7 (G) cells, represented as fold change in total colony area.

Each point represents an independent replicate. H-I, Brightfield (top) and fluorescence (bottom) images (H) and quantification (I) of spheroids formed by MDA-MB-231 cells under indicated conditions. GFP signal (green) marks expression positive cells within spheroids. Scale bar, 100 μm. J-K, Brightfield (top) and fluorescence (bottom) images (J) and quantification (K) of spheroids formed by MCF7 cells under the indicated conditions. Scale bar, 100 μm. Statistical significance was determined using one-way ANOVA (*p < 0.05, **p < 0.01, ***p < 0.001, ****p < 0.0001, ns, not significant).

Figure 4. Nup88-SENP3 axis enhances tumor formation and progression in vivo. A, Schematic representation of the xenograft experimental design showing subcutaneous injection of MDA-MB-231 cells stably expressing GFP constructs into NOD/SCID mice, followed by doxycycline-induced expression. B, Representative images of excised tumors from the indicated groups. Scale bar, 10 mm. C, Tumor growth curves showing tumor volume over time from the indicated tumor groups. D, Quantification of endpoint tumor weight from indicated groups. E, Quantification of endpoint tumor volume from indicated groups. Statistical significance was determined using one-way ANOVA for terminal analysis or two-way ANOVA for growth curve (*p < 0.05, **p < 0.01, ***p < 0.001, ****p < 0.0001). F, Experimental workflow for tumor cryosectioning and immunofluorescence analysis. G-H, Immunofluorescence images showing SENP3 (G) and Ki67 (H) in tumor sections derived from GFP and GFP-Nup88 overexpressing tissues.

Figure 5. Nup88 regulates ribosome biogenesis in a SENP3 dependent manner. A, Gene set enrichment analysis (GSEA) plot showing enrichment of rRNA processing pathways in Nup88-overexpressing tumor tissues from breast cancer patients. B-C,

RT-qPCR analysis of 47S pre-rRNA and 28S rRNA levels in indicated conditions. D-F, RT-qPCR expression analysis of ribosomal protein genes (*RPL28, RPL5, RPL11*) in indicated conditions. Data are presented as mean ± S.E.M. Statistical significance was determined using one-way ANOVA (*p < 0.05, **p < 0.01, ***p < 0.001, ****p < 0.0001). G, MDA-MB-231 cells with stable Nup88 expression system with/without induction with doxycycline for Nup88 overexpression (green), immunostained with RPL5 (red) and DAPI (blue). Scale bar, 10 μm. H, Flow cytometry histogram depicting RPL5 expression in stable MDA-MB-231 cell populations under indicated conditions. I, Overlay comparison of polysome profiles obtained under indicated conditions by sucrose gradient ultracentrifugation followed by absorbance measurement at 260 nm (A_{260}) across collected fractions. Peaks corresponding to the pre-polysomes and polysomes are indicated. J, Immunoblot analysis showing distribution of RPL5 across the collected fractions under indicated conditions. K, Correlation analysis between Nup88 and PELP1 expression in TCGA breast cancer datasets. L, Immunoblot analysis of PELP1 levels in MDA-MB-231 cells in indicated conditions. M, Immunofluorescence analysis in MCF7 cells analysing redistribution of PELP1 (red) upon Nup88 overexpression. Scale bar, 10 μm.

Figure 6. Nup88 mediates G1-S phase transition via CDK6 in a SENP3 dependent manner. A, Immunoblot analysis assessing CDK6 and SENP3 expression in MDA-MB-231 cells under the indicated conditions. GAPDH was used as a loading control. B-C, GSEA plots showing enrichment of E2F targets (B) and G2/M checkpoint (C) pathways in breast cancer patients' data with high Nup88. D-F, RT-qPCR analysis of E2F target genes (*CCNE1*, *TK1* and *NOP56*). G, Schematic for Palbociclib-based synchronisation and release of cells and downstream analysis. H, Representative cell

cycle distribution curves upon Palbociclib synchronisation and release of MCF7 under indicated conditions and time points by flow cytometry analysis. I, Quantification of (H) upon synchronisation-release of MCF7 cells at 12 hpr under indicated conditions. J, Immunoblot analysis detecting Rb phosphorylation (Ser780) upon Nup88 overexpression following 6 hpr. Data is represented as mean ± S.E.M. Statistical analysis was performed using one-way ANOVA; *p < 0.05, **p < 0.01, ***p < 0.001, ****p < 0.0001.

Figure 7. Proposed mechanistic model of Nup88 regulation in breast cancer. Schematic depicting a model in which elevated Nup88 enhances SENP3, thereby promoting ribosome biogenesis through increased ribosomal protein production (e.g. RPL5) and altered nucleolar organisation (e.g. PELP1). In parallel, Nup88 stimulates the CDK6-Rb-E2F signaling, facilitating cell cycle progression and contributing to tumor cell growth and proliferation. Intact arrows in the model represent findings of this study.

Figures

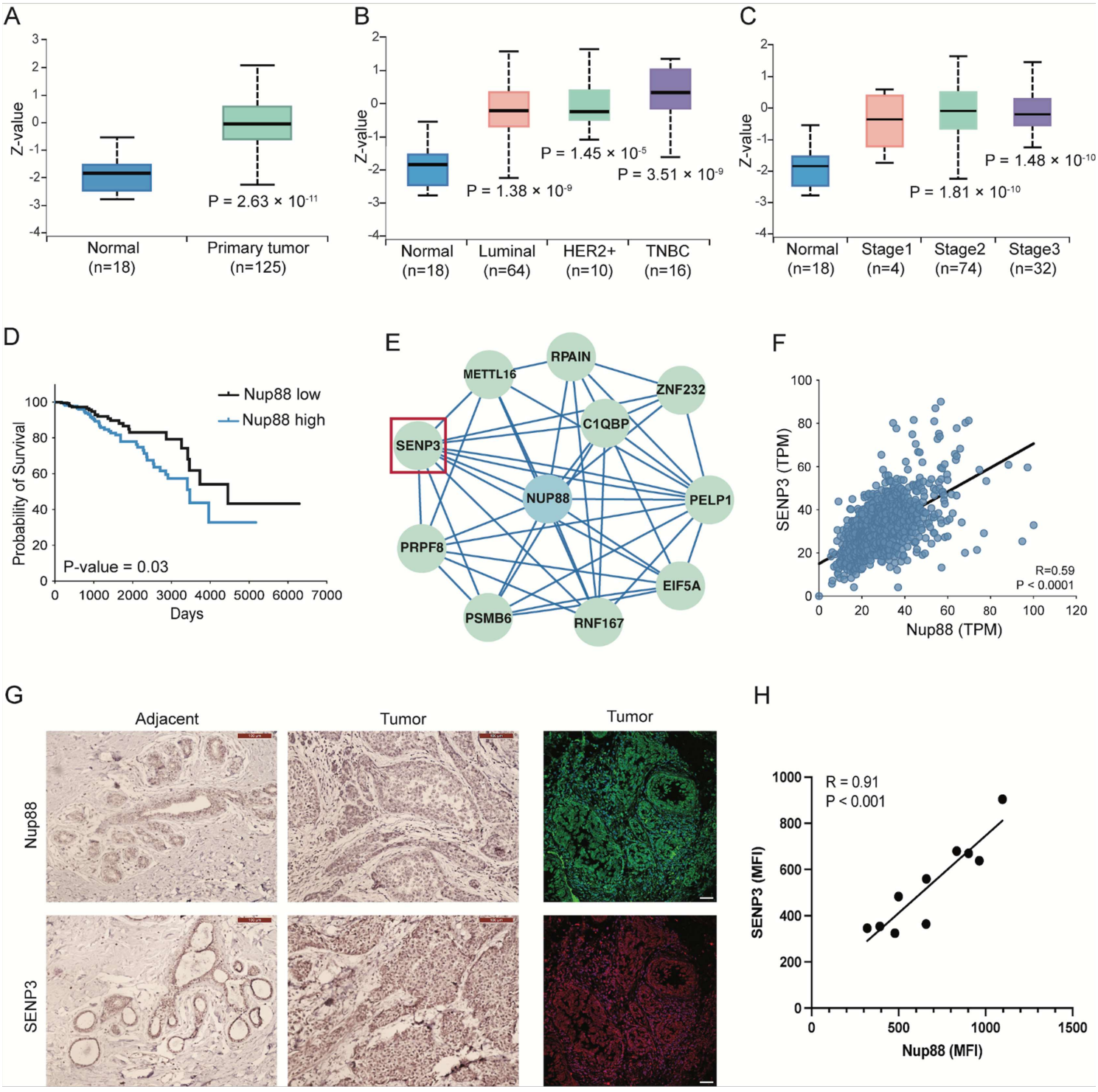


Figure 1

Nup88 is overexpressed in breast cancer and positively correlates with SENP3 expression. A, Nup88 protein expression in breast cancer tumor samples compared to normal tissue. B, Nup88 expression across breast cancer subtypes (Luminal, HER2+, and TNBC) compared to normal tissue. C, Nup88 expression across different stages of breast cancer progression. Statistical significance in (A-C) was

determined using unpaired t-test. D, Kaplan-Meier overall survival analysis of patients stratified based on Nup88 expression levels (low vs high). Statistical significance was determined using the log-rank test ($p = 0.03$). p-values are indicated in each case. E, Network analysis of Nup88-correlated genes in breast cancer (BRCA dataset), highlighting SENP3 as a significantly associated node. F, Scatter plot analysing correlation between Nup88 and SENP3 expression in breast cancer samples ($R = 0.59$, $p < 0.0001$). G, Immunohistochemical (IHC, left, Scale bar, 100 μm) and immunofluorescence (IF, right, Scale bar, 50 μm) analysis of Nup88 and SENP3 levels in breast cancer patient cohort. H, Pearson correlation analysis between Nup88 and SENP3 fluorescence intensities determined from IF ($R = 0.91$, $p < 0.001$, $n=10$).

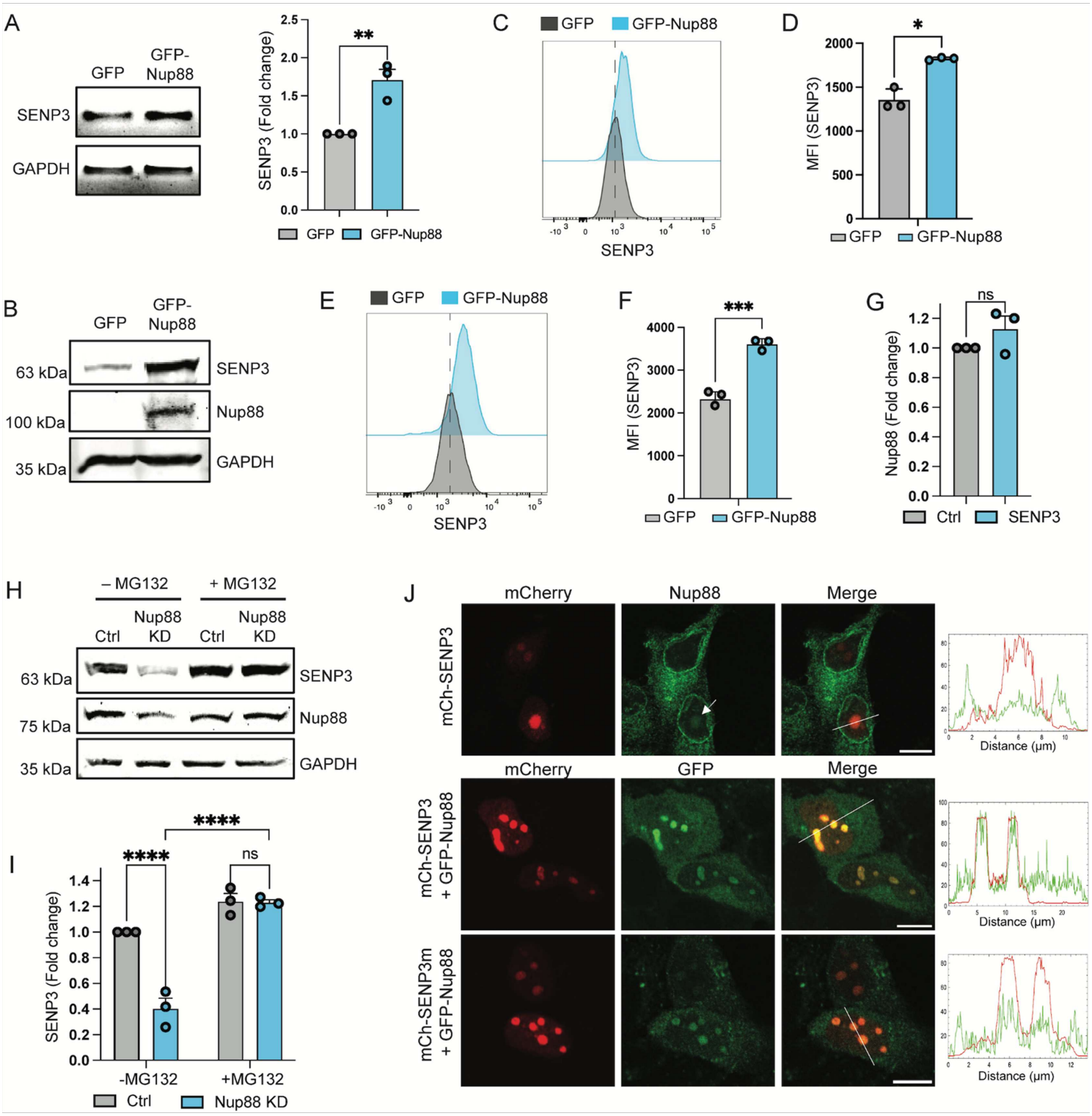


Figure 2

Nup88 regulates SENP3 stability and undergoes dynamic relocalisation through association with SENP3. A, Semi-quantitative PCR analysis and quantification of SENP3 levels in cells expressing GFP or GFP-Nup88. B, Immunoblot showing SENP3 levels upon GFP-Nup88 overexpression in MCF7. C, Flow cytometry histograms showing SENP3 expression in MCF7 with either GFP or GFP-Nup88 overexpression. D, Quantification of mean fluorescence intensity (MFI) of SENP3 under indicated conditions as in (C). E, Flow cytometry histograms showing SENP3 expression in MDA-MB-231 with

either GFP or GFP-Nup88 overexpression. F, Quantification of MFI of SENP3 under indicated conditions as in (E). Statistical significance in (A,D,F) was determined using unpaired t-test. G, Quantification of Nup88 levels upon SENP3 overexpression in MCF7. Statistical significance was determined using one-way ANOVA followed by Dunnett's multiple comparisons test. H, Immunoblot analysis of SENP3 levels upon shRNA-mediated Nup88 knockdown with/without MG132 (10 μM, 8 h) in MCF7 cells. I, Quantification of (H) showing fold change in SENP3 levels relative to control conditions. Statistical significance was determined using two-way ANOVA. Bars indicate mean ± S.E.M. (*$p < 0.05$, **$p < 0.01$, ***$p < 0.001$, ****$p < 0.0001$). J, Representative immunofluorescence image of MCF7 cells expressing either mCherry-SENP3 and stained for endogenous Nup88, or co-expressing mCherry-SENP3 and GFP-Nup88, or co-expressing catalytic mutant SENP3 (C532A) and GFP-Nup88. Line scans for images in merge panel are shown on the right. Scale bar, 10 μm.

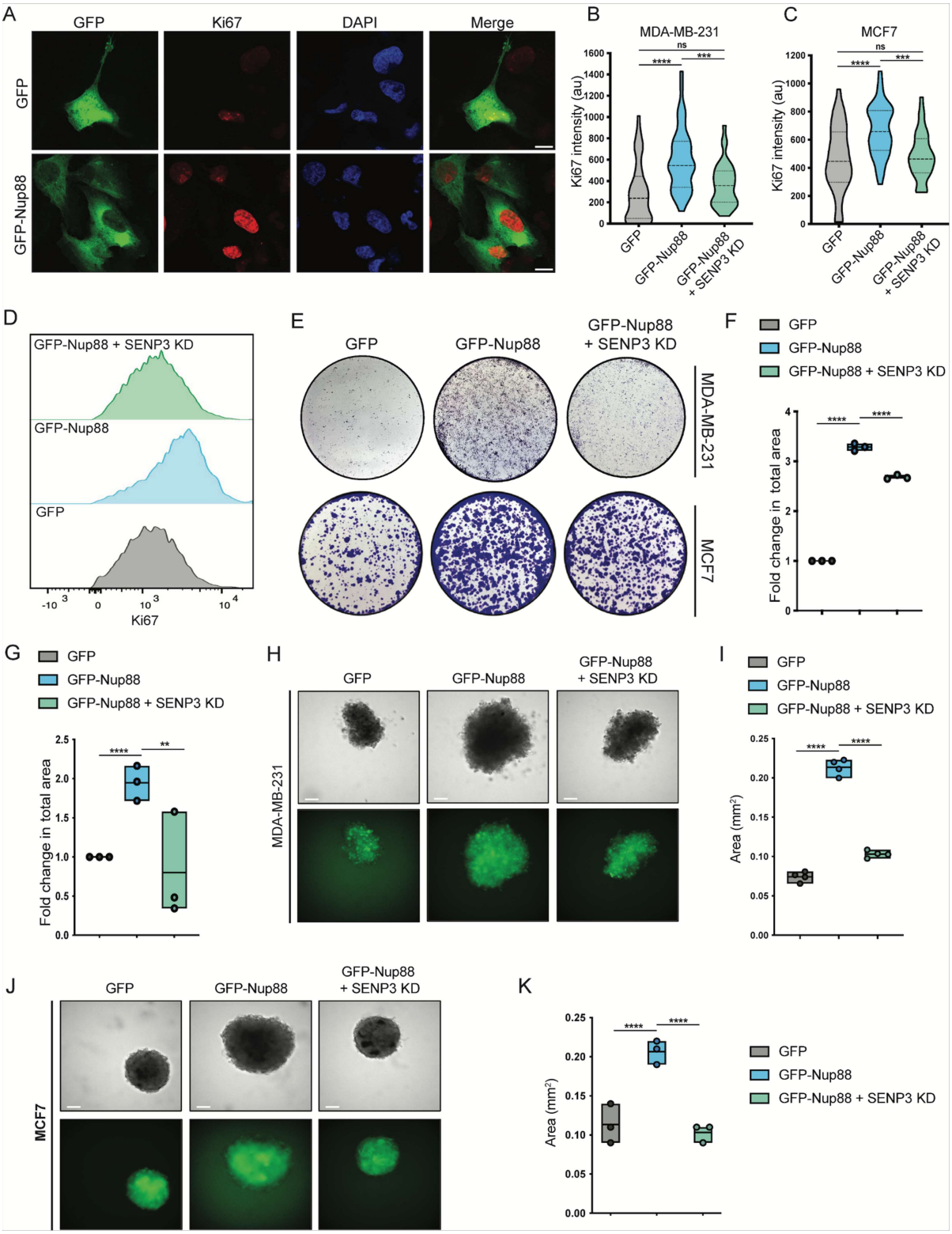


Figure 3

The Nup88-SENP3 axis promotes tumor proliferation in breast cancer cells. A, Immunofluorescence analysis of MDA-MB-231 cells expressing GFP or GFP-Nup88 (green) and stained for Ki67 (red) with DAPI (blue). Scale bar, 10 μm. B-C, Quantification of Ki67 fluorescence intensity in MDA-MB-231 (B) and MCF7 (C) cells under the indicated conditions, respectively. D, Flow cytometry histogram depicting Ki67 expression in MDA-MB-231 cell populations under indicated conditions. E, Representative images of

colony formation assay in MDA-MB-231 (upper) and MCF7 (lower) cells under indicated conditions. F-G, Quantification of colony-forming ability in MDA-MB-231 (F) and MCF7 (G) cells, represented as fold change in total colony area. Each point represents an independent replicate. H-I, Brightfield (top) and fluorescence (bottom) images (H) and quantification (I) of spheroids formed by MDA-MB-231 cells under indicated conditions. GFP signal (green) marks expression positive cells within spheroids. Scale bar, 100 μm. J-K, Brightfield (top) and fluorescence (bottom) images (J)and quantification (K) of spheroids formed by MCF7 cells under the indicatedconditions. Scale bar, 100 μm. Statistical significance was determined using one-way ANOVA (*p < 0.05, **p < 0.01, ***p < 0.001, ****p < 0.0001, ns, not significant).

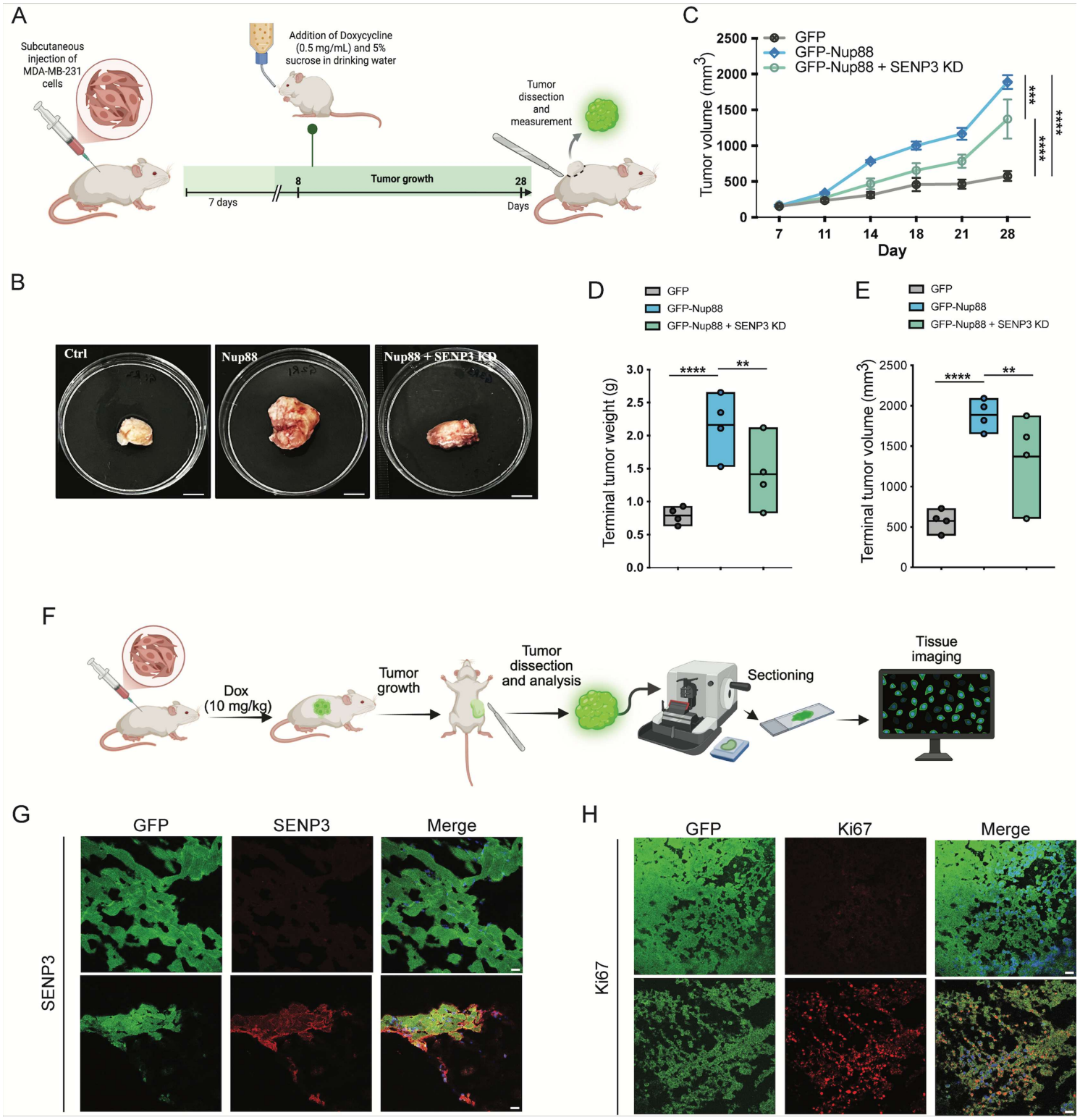


Figure 4

Nup88-SENP3 axis enhances tumor formation and progression in vivo. A, Schematic representation of the xenograft experimental design showing subcutaneous injection of MDA-MB-231 cells stably expressing GFP constructs into NOD/SCID mice, followed by doxycycline-induced expression. B, Representative images of excised tumors from the indicated groups. Scale bar, 10 mm. C, Tumor growth curves showing tumor volume over time from the indicated tumor groups. D, Quantification of endpoint

tumor weight from indicated groups. E, Quantification of endpoint tumor volume from indicated groups. Statistical significance was determined using one-way ANOVA for terminal analysis or two-way ANOVA for growth curve (*p < 0.05, **p < 0.01, ***p < 0.001, ****p < 0.0001). F, Experimental workflow for tumor cryosectioning and immunofluorescence analysis. G-H, Immunofluorescence images showing SENP3 (G) and Ki67 (H) in tumor sections derived from GFP and GFP-Nup88 overexpressing tissues.

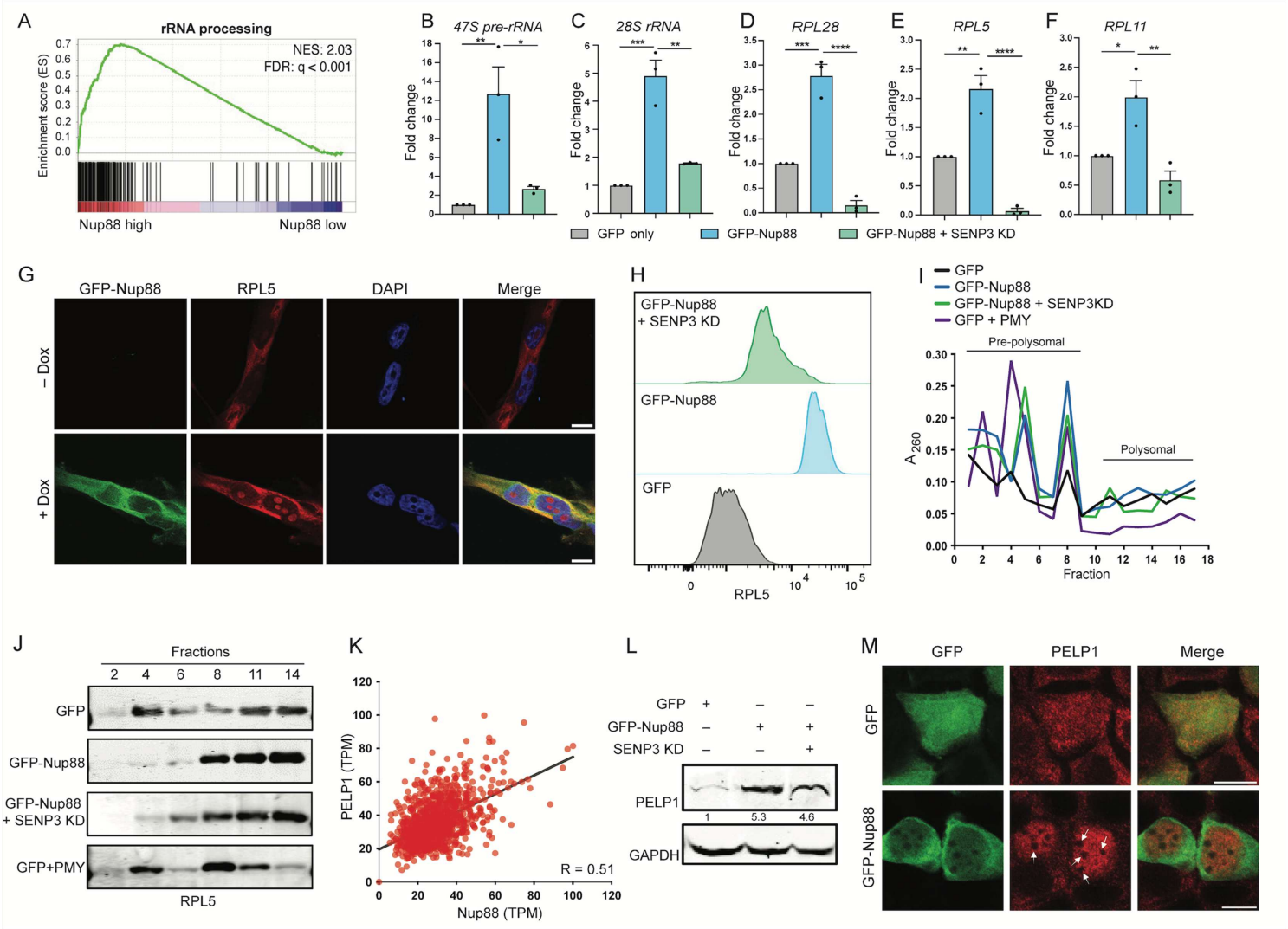


Figure 5

Nup88 regulates ribosome biogenesis in a SENP3 dependent manner. A, Gene set enrichment analysis (GSEA) plot showing enrichment of rRNA processing pathways in Nup88-overexpressing tumor tissues from breast cancer patients. B-C, RT-qPCR analysis of 47S pre-rRNA and 28S rRNA levels in indicated conditions. D-F, RT-qPCR expression analysis of ribosomal protein genes (RPL28, RPL5, RPL11) in indicated conditions. Data are presented as mean ± S.E.M. Statistical significance was determined using one-way ANOVA (*p < 0.05, **p < 0.01, ***p < 0.001, ****p < 0.0001). G, MDA-MB-231 cells with stable Nup88 expression system with/without induction with doxycycline for Nup88 overexpression (green), immunostained with RPL5 (red) and DAPI (blue). Scale bar, 10 μm. H, Flow cytometry histogram depicting RPL5 expression in stable MDA-MB-231 cell populations under indicated conditions. I, Overlay

comparison of polysome profiles obtained under indicated conditions by sucrose gradient ultracentrifugation followed by absorbance measurement at 260 nm (A260) across collected fractions. Peaks corresponding to the pre-polysomes and polysomes are indicated. J, Immunoblot analysis showing distribution of RPL5 across the collected fractions under indicated conditions. K, Correlation analysis between Nup88 and PELP1 expression in TCGA breast cancer datasets. L, Immunoblot analysis of PELP1 levels in MDA-MB-231 cells in indicated conditions. M, Immunofluorescence analysis in MCF7 cells analysing redistribution of PELP1 (red) upon Nup88 overexpression. Scale bar, 10 μm.

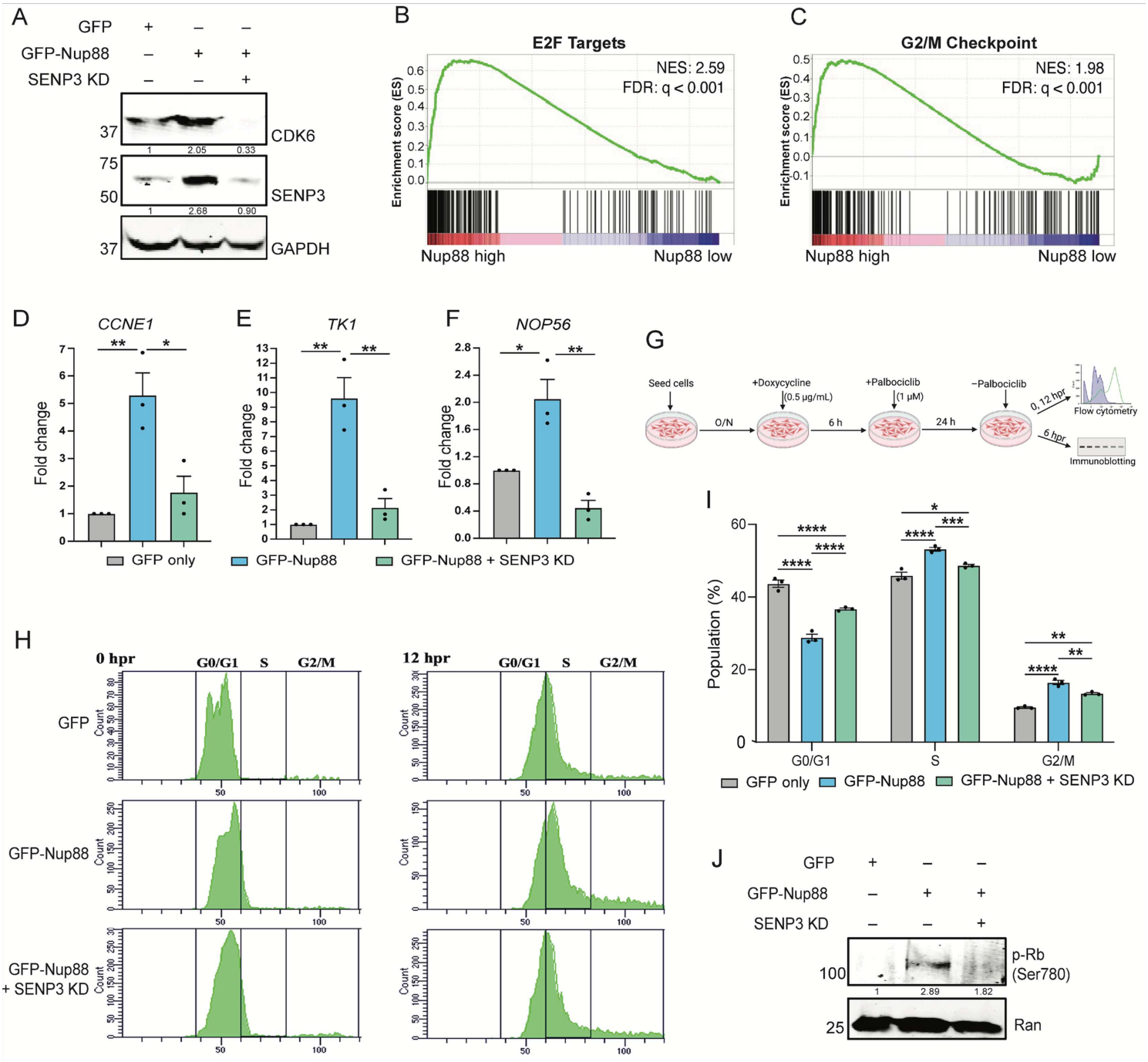


Figure 6

Nup88 mediates G1-S phase transition via CDK6 in a SENP3 dependent manner. A, Immunoblot analysis assessing CDK6 and SENP3 expression in MDA-MB-231 cells under the indicated conditions. GAPDH was used as a loading control. B-C, GSEA plots showing enrichment of E2F targets (B) and G2/M checkpoint (C)pathways in breast cancer patients' data with high Nup88. D-F, RT-qPCR analysis of E2F target genes (CCNE1, TK1 and NOP56). G, Schematic for Palbociclib-based synchronisation and release of cells and downstream analysis. H, Representative cell cycle distribution curves upon Palbociclib synchronisation and release of MCF7 under indicated conditions and time points by flow cytometry analysis. I, Quantification of (H) upon synchronisation-release of MCF7 cells at 12 hpr under indicated conditions. J, Immunoblot analysis detecting Rb phosphorylation (Ser780) upon Nup88 overexpression following 6 hpr. Data is represented as mean ± S.E.M. Statistical analysis was performed using one-way ANOVA; *p < 0.05, **p < 0.01, ***p < 0.001, ****p < 0.0001.

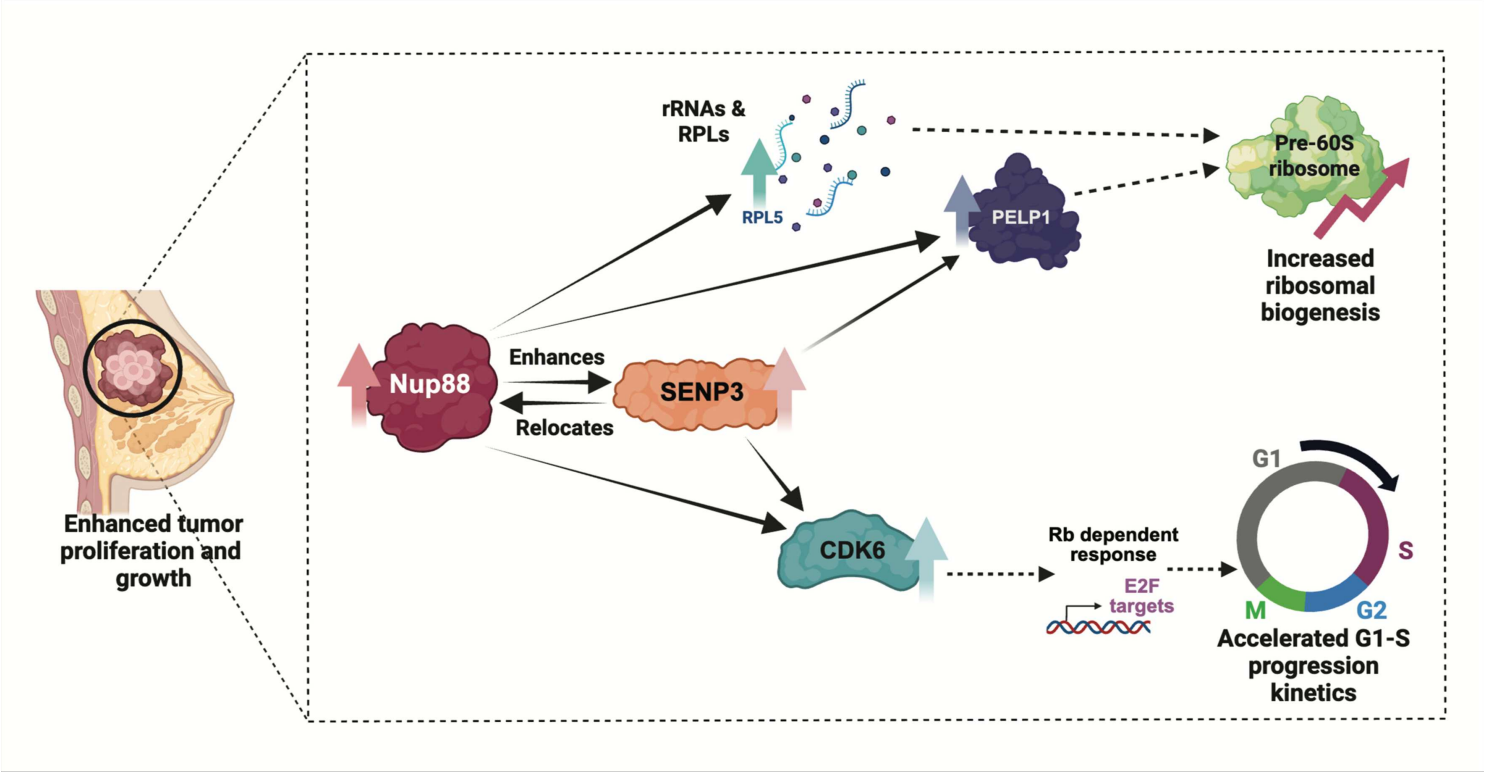


Figure 7

Proposed mechanistic model of Nup88 regulation in breast cancer. Schematic depicting a model in which elevated Nup88 enhances SENP3, thereby promoting ribosome biogenesis through increased ribosomal protein production (e.g. RPL5) and altered nucleolar organisation (e.g. PELP1). In parallel, Nup88 stimulates the CDK6-Rb-E2F signaling, facilitating cell cycle progression and contributing to tumor cell growth and proliferation. Intact arrows in the model represent findings of this study.

Supplementary Files

This is a list of supplementary files associated with this preprint. Click to download.

- SupplementaryFile1.pdf
- SupplementaryFile2.pdf
- SupplementaryTable1.xlsx
- SupplementaryTable2.xlsx
- SupplementaryTable3.xlsx